Ice resistance of hydrophobic fluoropolymerized nanostructured alumina films for antireflective coatings

To cite this article: Jarno Reuna *et al* 2022 *Nano Ex.* **3** 044002

NANO EXPRESS

PAPER

Ice resistance of hydrophobic fluoropolymerized nanostructured alumina films for antireflective coatings

Jarno Reuna[1], **Raul Kanter**[2], **Niklas Kandelin**[2], **Kaisa Kiuru**[2], **Heli Koivuluoto**[2] **and Mircea Guina**[1]

[1] Optoelectronics Research Centre, Physics Unit, Faculty of Engineering and Natural Sciences, Tampere University, PO Box 692, FIN-33014 Tampere, Finland

[2] Materials Science and Environmental Engineering, Faculty of Engineering and Natural Sciences, Tampere University, PO Box 692, FIN-33014 Tampere, Finland

E-mail: jarno.reuna@tuni.fi

OPEN ACCESS

RECEIVED
24 October 2022

REVISED
9 December 2022

ACCEPTED FOR PUBLICATION
19 December 2022

PUBLISHED
4 January 2023

Keywords: alumina, nanostructure, icing, hydrophobic, antireflection

Abstract

The functionality and durability of nanostructured alumina coatings exposed to atmospheric icing has been assessed to probe their usability in practical applications and to estimate the need for further development of the coatings. In particular, the changes in surface microstructure and in optical performance as well as in the wetting characteristics of the surfaces are reported. Without a hydrophobicity treatment the alumina nanostructures are superhydrophilic and do not endure large environmental changes. Hydrophobicity treated fluoropolymerized nanostructured alumina provides characteristics with partial anti-icing capabilities, enhanced durability, and excellent transmission levels of >95%, but the performance degrades in cyclic icing/de-icing. However, the hydrophobic nanostructured alumina outperforms both the nanostructured and planar alumina coatings and possesses increased durability and stability even under harsh conditions, such as the atmospheric icing. This indicates a clear need to use a hydrophobicity treatment for the nanostructured alumina antireflection coatings to be used in any environments. Therefore, its utilization in applications where little or occasional exposure to icing or other humidity and temperature changes is favorable over standard planar coatings. Further process optimization of the hydrophobicity treatment is still needed for better durability for cyclical icing exposure.

1. Introduction

The use of nanostructured alumina antireflection coatings (ARC) have lately attracted scientific attention [1–7] owing to the simple and low-cost fabrication method, where an amorphous alumina thin film is nanostructured by a heated deionized water (DIW) treatment. The proven suitability of the method for general optics and applications [2, 4] and solar cell coatings [1, 3, 5] makes this approach an appealing alternative to the established methods for fabricating nanostructured broadband ARCs, which generally speaking are more laborious [8–16]. On glass surfaces the nanostructured alumina ARCs have enabled an average transparency as high as 99% at visible wavelengths [1, 2] on both sides coated substrates. Furthermore, it is possible to combine the nanostructured alumina with conventional planar coatings to expand the spectral bandwidth of the low reflectivity and to match the refractive index to high index substrates such as semiconductors [2, 3]. As alumina can be conformally deposited by atomic layer deposition [1, 17–19] and planarly by any physical vapor deposition method [2, 20–23] or sol-gel method [6, 24–27], it is applicable to any type of surface. To increase the stability of the nanostructures, superhydrophobicity treatments are often applied [28–34]. These are typically based on providing an additional low surface energy polymer, such as organosilane [6, 28, 30], fluoropolymer (PTFE) [28, 32, 35], or polydimethylsiloxane (PDMS) [29, 34] on top of the nanostructures. Similarly, we have used a fluoropolymerization by CHF_3 plasma to potentially enhance the durability of the coating [5]. However, the search for other polymers is still active because CHF_3 is a potent greenhouse gas [36], while the fluoropolymers bring potential health and environmental risks [37, 38], making it non-compatible for large scale applications.

When used in solar panel cover glasses [6] and solar cells [39], the coatings are often exposed to ambient conditions in which both humidity and temperature variations can cause degradation of the optical and mechanical properties. Therefore, it is necessary to test the durability of the nanostructured alumina ARCs and evaluate their long-term stability for real-life applications. As the atmospheric icing, a state in which surface exposed to super-cooled water droplets accumulates ice, is one of the harshest environmental conditions and can lead to extensive structural damage for the surfaces, we have chosen to test the nanostructured alumina under these conditions to promote accelerated aging and wear on the coatings. It is expected that the hydrophobicity treated nanostructures will not act as a permanent anti-icing coating [40–42] due to the frost formation via condensation [43, 44], which will wear out the nanofeatures on the surface [45]. The comparison should, however, reveal the differences between the coating types, the regular planar film, the bare nanostructure, and the fluoropolymer coated nanostructure, and show whether a hydrophobicity treatment is a necessity for the durability of the alumina nanostructures.

We find it crucial to investigate the stability of the nanostructured alumina ARCs to enable their use in practical applications and to assess the need for further development of the coatings. To this end, we fabricated nanostructured alumina films with and without the CHF_3 hydrophobicity treatment and compared their performance to planar alumina films on glass and silicon. The films were exposed to the atmospheric icing in an icing laboratory, characterized prior and after the ice accretion, and a centrifugal adhesion test was implemented to investigate the durability of the coatings under these conditions.

2. Methods

2.1. Alumina deposition and coating modifications

A test series of 25 nm thick Al_2O_3 films was deposited on diced silicon wafer pieces (0.5 mm × 30 mm × 35 mm) and glass slides (0.5 mm × 30 mm × 35 mm) using a Navigator 700 sputtering system (Cutting Edge Coatings GmbH). Sputtering was performed using an Ar:O_2 mixture with the flow rates of 8 sccm to 5 sccm, respectively. The deposition took place in a reactive O_2 atmosphere with a pressure of 4.5×10^{-4} mbar. A 200 × 200 mm aluminum plate with a purity of 99.999% was used as the target. The sputtering voltage was 1.26 kV, and the RF power of the ion source was 102 W. During the deposition, the sample holder was rotated at 60 rpm to guarantee uniform deposition.

One third of the samples were examined as deposited and they are referred as 'Plano' samples. The rest of the samples were immersed in a non-stirred heated (90 °C) DIW bath for 30 min to produce the nanostructured Al_2O_3. More detailed description of the nanostructuring process can be found in the [2]. Half of the DIW treated samples were investigated without further processing and are referred as 'Nano' samples. The remaining third of the samples were fluoropolymerized [5] to provide hydrophobicity by using a reactive ion etcher (RIE) Plasmalab 100 (Oxford Instruments Plasma Technology GmbH). The polymerization was done with CHF_3 plasma (50 sccm, 100 mTorr, 50 W) for 7 min. This third of the samples is further referred as 'Fluoro' samples. Figure 1 provides an overview of the fabrication steps for the sample series. Each of the sample types comprised four similar samples for statistical measurements.

In addition to the naming by the coating type (Plano, Nano, Fluoro) we also refer to the substrate in question as silicon (Si) and glass to distinct the differences between the coated surface types.

2.2. Ice accretion and centrifugal adhesion testing

For icing tests, a mixed glaze type ice was accreted by using an icing wind tunnel (IWiT) at TAU/Ice Laboratory. A centrifugal ice adhesion tester (CAT) was used for ice adhesion measurements [46]. Both test systems have been placed in cold climate room, where the temperature was −10 °C and relative humidity was ∼80%. Supercooled water droplets were accelerated to the surfaces, and they were frozen on the surface. The water droplet diameter size was ∼30 μm and the droplet speed was 25 m s^{-1}. For ice adhesion tests, the samples were kept in the cold condition ∼16 h before CAT testing to ensure full freezing. For the CAT, an ice layer was accreted on the test surfaces of the size of 30 × 30 mm. The thickness of the accreted ice was ∼10 mm. During the adhesion test, the iced sample is rotated with a constant acceleration speed until the ice layer detaches. An acceleration sensor logs the detachment moment, and the ice adhesion strength can be calculated by dividing the centrifugal force with the iced area. More information on this process can be found in the [46–49]. Four parallel samples of each coating type were tested, and the results are given as averages with the standard deviations. The defined ranges for the measured ice adhesion forces are:

- Extreme low <10 kPa
- Low 10–50 kPa

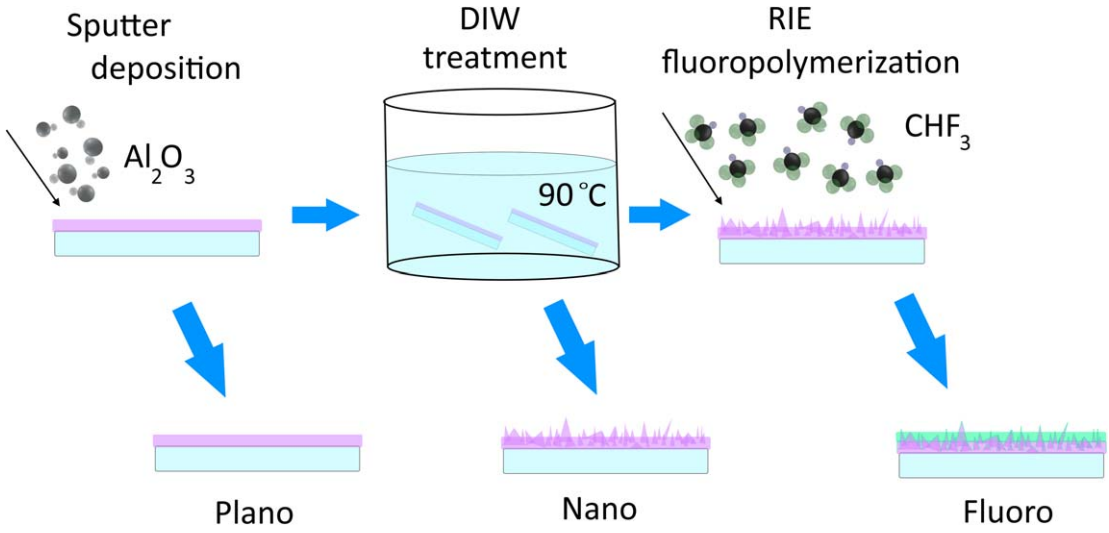

Figure 1. The fabrication process of the sample series, where Plano is the planar alumina coating, Nano is the nanostructured alumina film and Fluoro is Nano treated with CHF_3 plasma.

- Medium-Low 50–100 kPa
- Medium 100–150 kPa
- High >150 kPa

Ice durability tests were done after CAT testing. In these tests, ice was accreted on the surface in IWiT following the same procedure as for CAT testing. After the ice accretion, the samples were left to the cold conditions to freeze for one hour. Afterwards, the de-icing was done at the room temperature. In the de-icing, the samples were positioned vertically and held there until the ice was removed by melting. This procedure was repeated four times, after which water contact angles were measured to indicate possible changes in the surface wetting behaviour.

2.3. Characterization of the coating properties

Prior and after the CAT icing the samples were characterized to determine performance changes caused by the rapid freezing and the ice removal in the adhesion testing. Scanning electron microscope (SEM) images were taken with an Ultra-55 FESEM operated with SmartSEM® software, both products of Carl Zeiss NTS Ltd. The used acceleration voltage was 1 kV, and the aperture size was 10 μm. For surface roughness measurements a Dimension™ 3100 Atomic force microscope (AFM) from Veeco Ltd was used and the AFM image data was constructed with WSxM 5.0 Develop 9.4 software [50]. A PerkinElmer Lambda 1050 UV/VIS/NIR spectrophotometer equipped with an integrating sphere was used for the reflectance and transmittance measurements. In addition to the specular reflectance and transmittance, integrating sphere nominally measures also the scattered light.

The water contact angles were measured to evaluate the wetting behaviour of the surfaces. Static and dynamic contact angles were measured with a droplet shape analyser (DSA100, Krüss, Germany) in the controlled temperature of 22 °C and a relative humidity of 50%. Measurements were done with 5 μl droplets of ultra-high purity water (MilliQ, Millipore Corporation, USA). Static, advancing and receding contact angles are given as an average of nine measurements with the standard deviations. Hysteresis is calculated as a difference between the advancing and receding angles. The contact angle values were measured before icing tests, after the CAT testing, and after the cyclic icing/de-icing durability tests. For planar surfaces the contact angle represents the surface tension ratio between the different states, as is stated by the Young's equation [51]:

$$\cos\theta = (\gamma_{SV} - \gamma_{SL})/\gamma_{LV}, \quad (1)$$

where θ is the contact angle and γ_{SV}, γ_{SL}, are the interfacial surface tensions for the solid-vapor, the solid-liquid and the liquid-vapor interfaces, respectively. The relation between the magnitude of the contact angle and the hydrophilicity/-phobicity on a planar surface is illustrated in figure 2(a).

For the nanostructured coating the relations between the surface, the contact angle and the surface tension are not as straightforward, as the droplet has a different contact area with the surface than with the planar counterpart, which is illustrated in figure 2(b). There are two different states the droplet can be in: the Wenzel

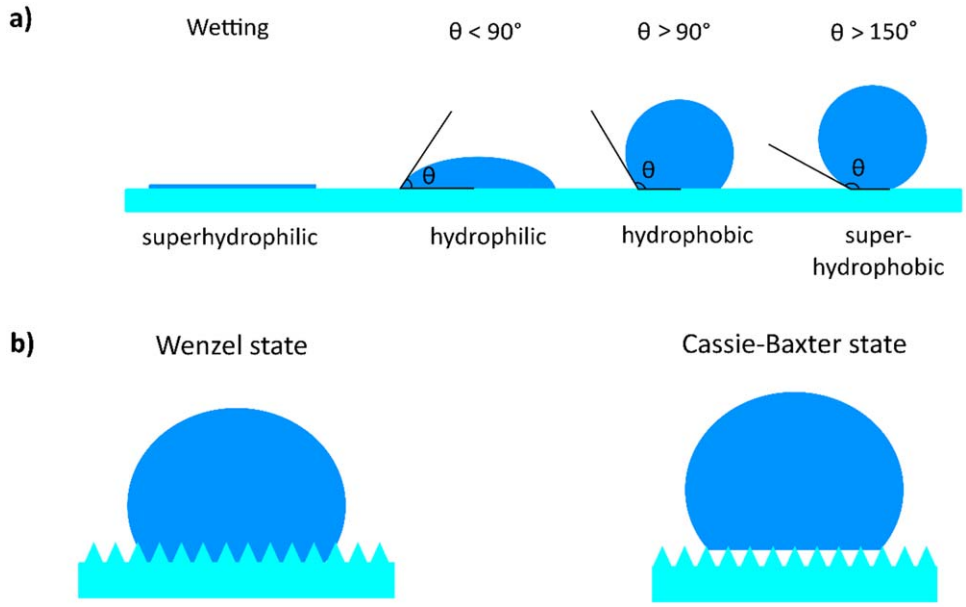

Figure 2. (a) A schematic illustration of the static water drop contact angles from superhydrophilic to superhydrophobic state [52, 53]. (b) A schematic representation of a water droplet on a structured surface in the Wenzel state [54, 55] where the droplet is immersed within the structure and in the Cassie-Baxter state [56] where the surface tension keeps the droplet elevated on top of the structure.

state [54, 55] in which the droplet is completely merged within the nanostructure, making its contact area larger than the geometric area its covering. Or the Cassie-Baxter state [56] where the droplet stays elevated on the nanostructure having voids of air underneath. In the Cassie-Baxter state, the area between the coating and the droplet is significantly smaller than with the planar coating. For a droplet in the Wenzel state the corrected contact angle θ^* can be estimated as [54, 55]:

$$\cos\theta^* = R\cos\theta = \frac{A_{textured}}{A_{planar}}\cos\theta, \tag{2}$$

where R is the ratio of the textured and the planar surface areas, $A_{textured}$ and A_{planar}, respectively. Similarly, for the Cassie-Baxter state [56] can be written:

$$\cos\theta^* = -1 + \varphi_S(\cos\theta + 1), \tag{3}$$

where φ_S is the solid fraction of the surface. During the contact angle characterization, we qualitatively analyse of which state the surface/droplet pair is in, as based on the work of Kulinich *et al* [45] even hydrophobic nanostructures, that follow Cassie-Baxter state, wear out and will at some point switch to Wenzel state [44]. Furthermore, the states are not explicit, so the distinctions made are to be taken as indicatives only. However, they provide a useful categorizing for the surface property analysis [57–59].

3. Results and discussion

To determine what type of hydrophobicity/-philicity the coatings possess, the static water contact angles (SCA) were measured prior the icing. Figure 3(a) shows that Plano coatings on both the surfaces are hydrophilic in nature (SCA $< 90°$) [52]. Similarly, it is seen that Nano samples are superhydrophilic, as the droplets spread out on the surfaces immediately [53], which indicates Wenzel state for its tension mechanism. Fluoro samples are hydrophobic (SCA ~130°), but not superhydrophobic likely putting them in Cassie-Baxter state. In overall, the coating performance is very similar between the two substrate materials.

The samples were iced, and the ice was removed with the centrifugal adhesion test. Figure 3(b) shows the measured ice adhesion values for the alumina coatings. The exact icing conditions and descriptions for the different adhesion strength ranges from extreme low to high were presented in the methods. There seems to be no significant effect of the substrate material on the ice adhesion, which indicates similar growth and nanostructuring process for the alumina coatings on both the substrates. Plano samples have ice adhesion strengths of nearly 70 kPa, which corresponds to the medium-low adhesion region. Nano samples exhibit adhesion values of 60 kPa that corresponds to the same adhesion level than Plano samples have. Therefore, the nanostructuring has a relatively small influence on the ice adhesion. Fluoropolymerization reduces the ice

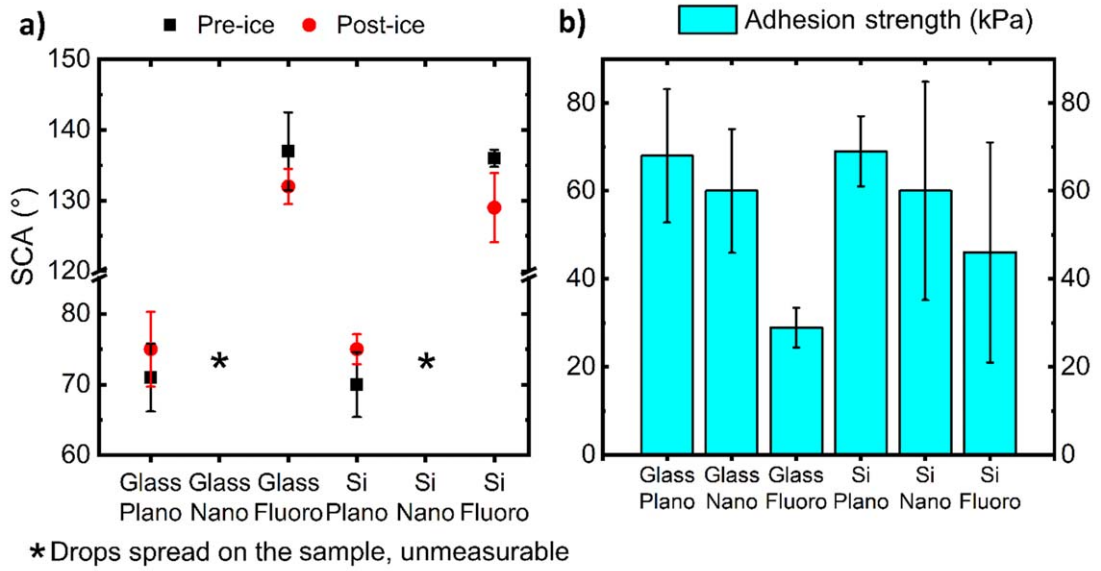

Figure 3. (a) The static water contact angles before and after the ice adhesion test. (b) The measured ice adhesion values with the centrifugal adhesion test. The error bars represent the standard deviation of the measurements.

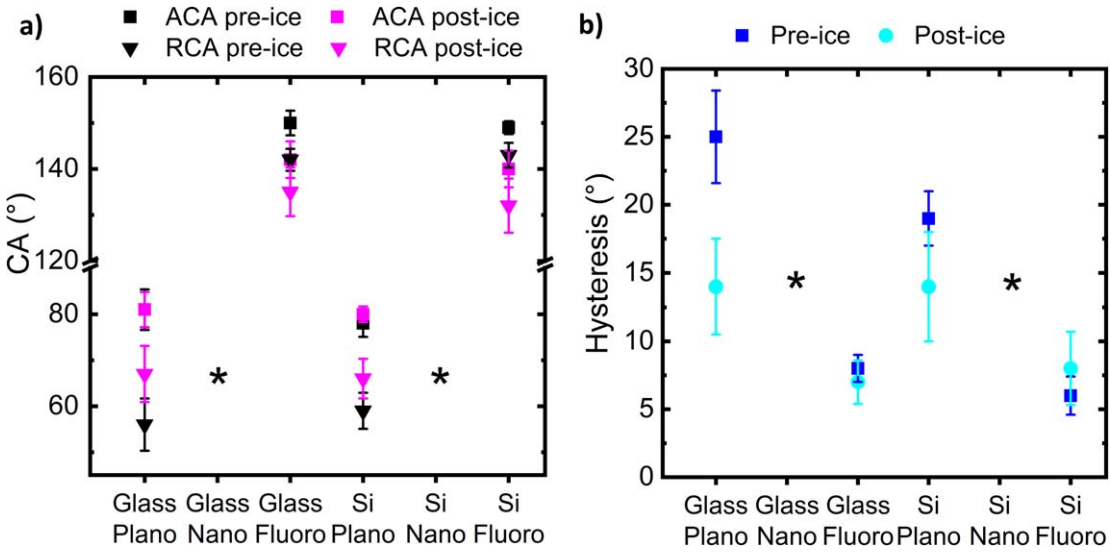

Figure 4. (a) The dynamic contact angles, as the advancing contact angle (ACA) and the receding contact angle (RCA) before and after the ice adhesion test. (b) The contact angle hysteresis before and after the ice adhesion test. *Drops spread on the sample, unmeasurable.

adhesion significantly more and the corresponding values for Fluoro on glass and on silicon are 29 kPa and 46 kPa, respectively. Both surfaces reach the low adhesion region. The low ice adhesion achieved with the fluoropolymerized nanostructured alumina is excellent in the light of the reported anti-icing coatings having values between 50 kPa to over 100 kPa [28, 30, 31, 33, 60], although lower values (~10 kPa) have also been presented [34].

While SCAs are typically used as the standard for hydrophobicity evaluation, statistical analysis done by Law *et al* [52, 61] suggests that the receding contact angle (RCA) is more suitable choice for the limit value of 90° between hydrophobicity and hydrophilicity. Generally, RCA is a measure for the surface adhesion and the advancing contact angle (ACA) measures the surface wettability [52, 61]. CA hysteresis is the difference between RCA and ACA and is mostly due to chemical and topographical heterogeneity of the surface, or surface alteration by the solution [62, 63]. As RCA and ACA give the local maximum and minimum values that SCA can have on the surface, smaller hysteresis indicates more stable and uniform performance by the coating.

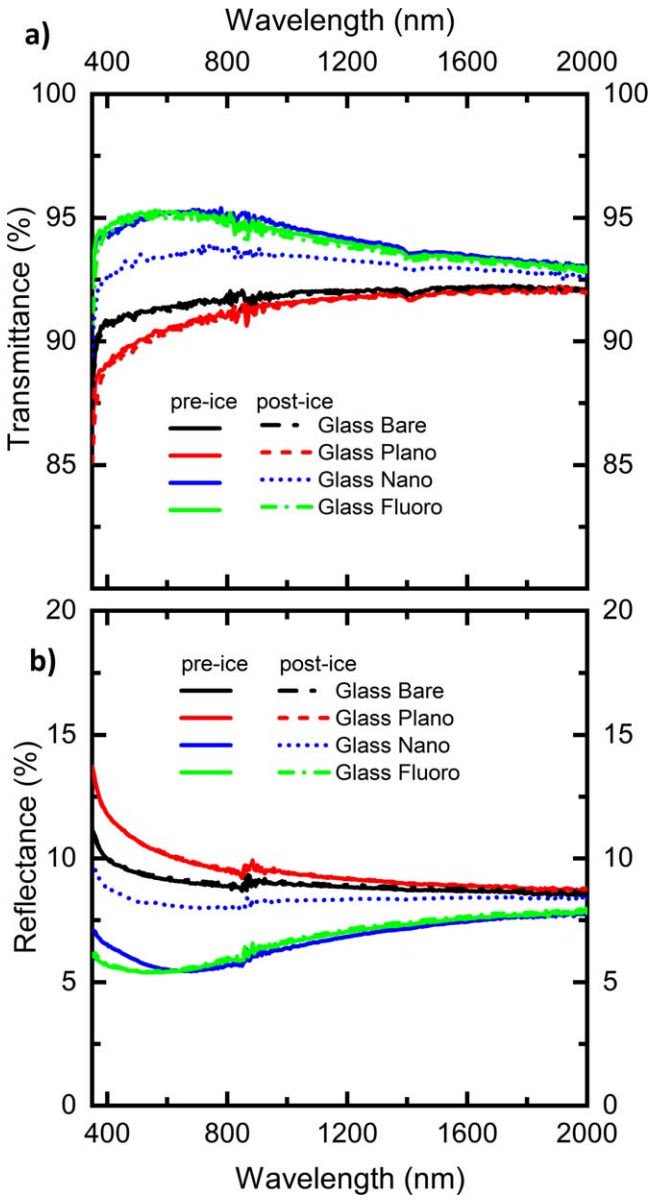

Figure 5. (a) Transmittance of the alumina films on glass before and after the ice adhesion test at the normal incidence. (b) Reflectance of the alumina films on glass before and after the ice adhesion test at the normal incidence.

Figure 4(a) provides the dynamic CAs for alumina surfaces prior and after icing and figure 4(b) shows the corresponding CA hysteresis.

Both ACA and RCA values for Fluoro samples are somewhat higher than the SCAs, but the range remains as hydrophobic and not superhydrophobic. For Plano samples, ACAs are larger than SCAs and RCAs smaller than SCAs, which explicitly leads to larger hysteresis. The trend of change for both ACAs and RCAs after icing is similar to SCAs, so there is a reduction for both of a few degrees for Fluoro samples. The hysteresis for Fluoro samples is relatively low ~7° both prior and after icing and indicates more stable surface properties when compared to Plano samples that exhibit values above 10°.

When used as an antireflection coating, the average transmittance, reflectance, and their changes due to the icing de-icing procedure are of great interest. Especially for multijunction solar cells and their cover glasses, the broadband operation needs to remain un-altered to prevent changes in the current-balancing of the junctions [64, 65]. For the solar cell cover glasses the antireflective properties of the nanostructured alumina is sufficient on its own, while for semiconductors, like silicon, the alumina nanostructure can be combined with underlying multilayer ARC to achieve low enough reflectance [2, 3]. Therefore, the focus here is on revealing any notable changes in performance due to the icing and the abrupt de-icing. The transmittance of Plano, Nano, and Fluoro on glass, both pre-iced and post-iced, are shown in figure 5(a). Their reflectance is shown in figure 5(b). The bare glass was not iced and is presented as a reference for the measurement coherence. The average pre-ice transmittance over the bandwidth of 400 nm to 800 nm for Plano, Nano, and Fluoro are 90.4%, 95.0%, and

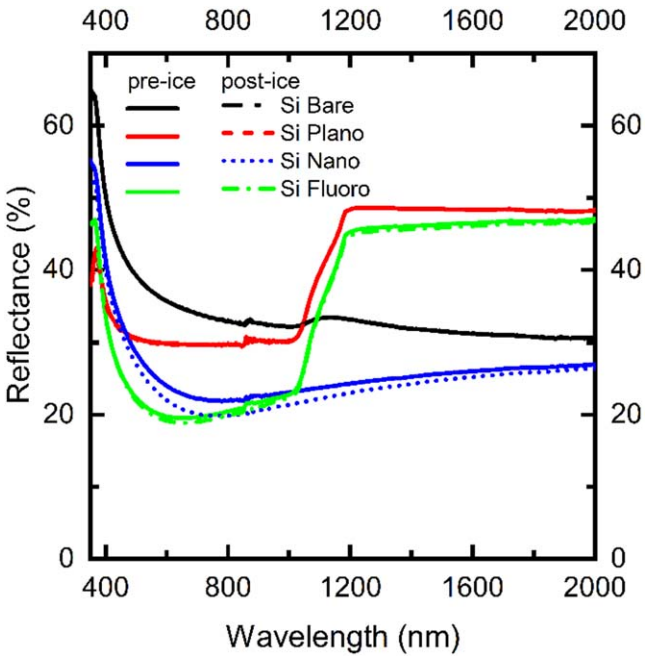

Figure 6. Reflectance of the alumina films on silicon before and after ice adhesion test at the normal incidence.

95.1%, respectively. Compared to many other hydrophobic and anti-icing coatings the presented transmittance of ~95% is excellent, as the reported transparencies are usually reduced ~1%–10% from the bare glass transmittance at similar bandwidths [29, 30, 34, 60]. There are also no losses involved in the coatings as the transmittance and reflectance sum-up to 100% over the examined bandwidth.

When comparing the changes between the pre-iced and post-iced samples both in transmittance and reflectance, it is seen that only Nano has been significantly influenced by the icing. The transmittance of Nano has reduced, and reflectance increased, so presumably the nanostructure has been altered due to the icing. The biggest effect on Nano is at the visible wavelengths, where the change in reflectance is on average 2.5% and for transmittance 1.6%. Similar changes are not seen with Fluoro, so the hydrophobicity seems to provide at least a momentary protection against the effects of the atmospheric icing.

The reflectance of alumina coatings on silicon are presented in figure 6. In overall, the icing and the removal of ice with the centrifugal adhesion test seems to affect only the reflectance of Nano. Otherwise, the measured values for the pre-ice and the post-ice samples are of the same order. For Nano the reflectance has dropped 1.8% at 400–800 nm, which would indicate changes in the nanostructure due to the icing procedure.

In addition to the surface reflectance from the coated side, there is an apparent backside reflectance of the silicon substrate for Plano and Fluoro samples. As the DIW treatment is known to etch silicon [66], it could cause etching of the uncovered backside of the wafers and lead to smoothening them to mirrorlike surface. However, Plano was not DIW treated and Nano, which does not have any back side reflectance, was. It is more likely that the difference in the backside reflectance is due to the initial quality variations of the silicon substrates.

The surface microstructure and topography of the alumina coatings were examined by AFM to see the effects of icing on the coating structure. Figure 7 presents the topographical surfaces of the pre- and the post-iced Plano, Nano and Fluoro, (a)–(b), (c)–(d), and (e)–(f) on glass, respectively. The root-mean square roughness of the nanostructured Nano and Fluoro is of the order of ~35 nm, which is significantly smaller than roughness of the regularly used antireflective or anti-icing nanostructures, that usually have R_{rms} ranging between 200 and 400 nm [28, 31, 60, 67]. For Plano there is some nominal roughening of the surface due to the icing and the adhesion test process, but otherwise the surface is micro-structurally unchanged. For Nano the change is drastic. Practically all the nanostructured alumina has been ripped off with the ice during the adhesion test and only small islands with a height of ~20 nm are still visible on the image. As these AFM scans were relatively small areas (3×3 μm), Nano sample was measured from several spots to rule out only local delamination of the coating. Observations confirmed that the nanostructure has consistently come off from the glass substrates. It is now clear that just nanostructured alumina on glass is not suitable for conditions where there is possibility to be exposed to icing. In contrast, Fluoro samples show little to no evidence of delamination or other major structural alterations. Like Plano sample, there is only minor roughening based on the statistical roughness values. Altogether the alumina nanostructure on Fluoro raises hopes for an environmentally stable ARC for glass even under harsh conditions.

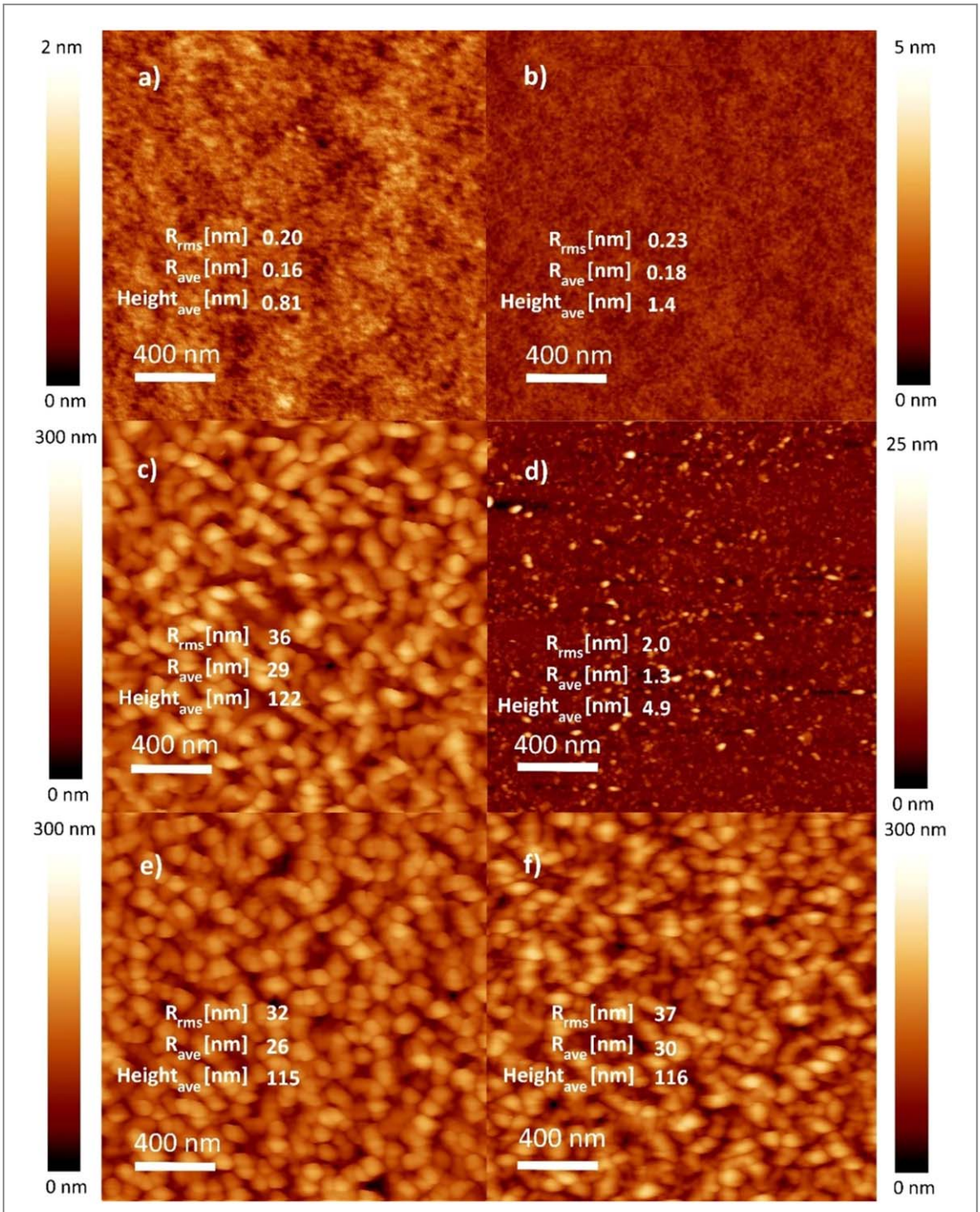

Figure 7. The surface topography maps of alumina films on glass measured with AFM. (a) shows the planar alumina (Plano) film prior the icing and (b) after the ice adhesion test. (c) Nano sample before the icing and (d) post the ice adhesion test. The pre-iced fluoropolymerized sample (Fluoro) is shown in (e) and the post-ice adhesion test in (f).

In figure 8 are presented the topographical surfaces of the pre- and the post-iced Plano, Nano and Fluoro, (a)–(b), (c)–(d), and (e)–(f) on silicon, respectively. The pre-iced surfaces are very similar to the coatings on glass, but the nanostructured surfaces seem to have few nanometers smaller average heights than Nano and Fluoro on glass. Plano on silicon has also just slight roughening as was on glass, but Nano sample deviates from the glass counterpart. As it happens, Nano on silicon has not peeled off, but maintains its nanostructure. The features seem sharper in contrast than before the icing and there is some increase in roughness values, but the nanostructure has not notably changed. Apparently, the adhesion of alumina on silicon is greater than the adhesion on glass, as the measured adhesion of ice on Nano on both substrates was basically the same (~60 kPa).

AFM scans provide information from a very specific area of the sample surface, so to get a wider overview of the surface quality the coatings were imaged with SEM. Because insulating and transparent samples like glass are more difficult to image with SEM, only coatings on silicon were imaged. Figure 9 presents selected pre-iced

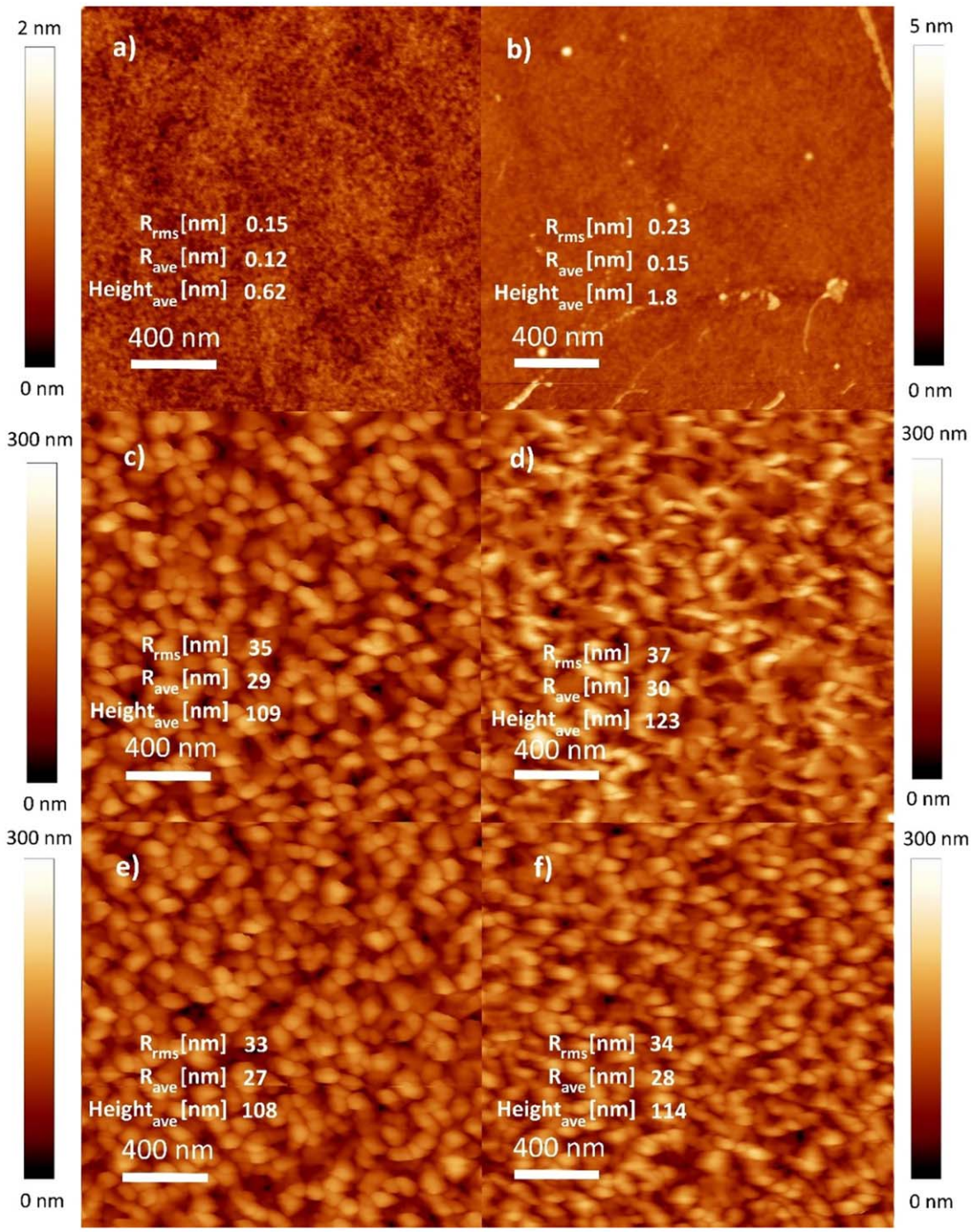

Figure 8. The surface topography maps of alumina films on silicon measured with AFM. (a) shows planar alumina (Plano) film prior the icing and (b) after the ice adhesion test. (c) Nano sample before the icing and (d) the post icing. The pre-iced fluoropolymerized sample (Fluoro) is shown in (e) and the post-iced in (f).

Plano, Nano, and Fluoro surfaces in (a)–(c), respectively, and post-iced Plano, Nano, and Fluoro in (d)–(f), respectively.

All of the three pre-icing surfaces are uniform and for the nanostructured Nano and Fluoro samples the surface topography looks the same. The contrast difference in the figures 9(b) and (c) subplots is the main give-away of the additional fluoropolymer on the surface of Fluoro sample. The dark spots in Plano sample are not holes or islands but seemingly inner inconsistencies in the films. It is possible that the features would originate from the silicon substrate or density variations in the film. After the icing and removing the ice with the centrifugal adhesion test, all three surfaces show some differences. Plano sample has micrometers wide areas where the coating has been ripped off and there are some micro-cracks near such areas. Nano sample has mainly the same structure than before the icing and the nanostructure seems to be unchanged. However, there are large holes with diameters ranging from 1 μm to tens of micrometers of which the coating has completely peeled off

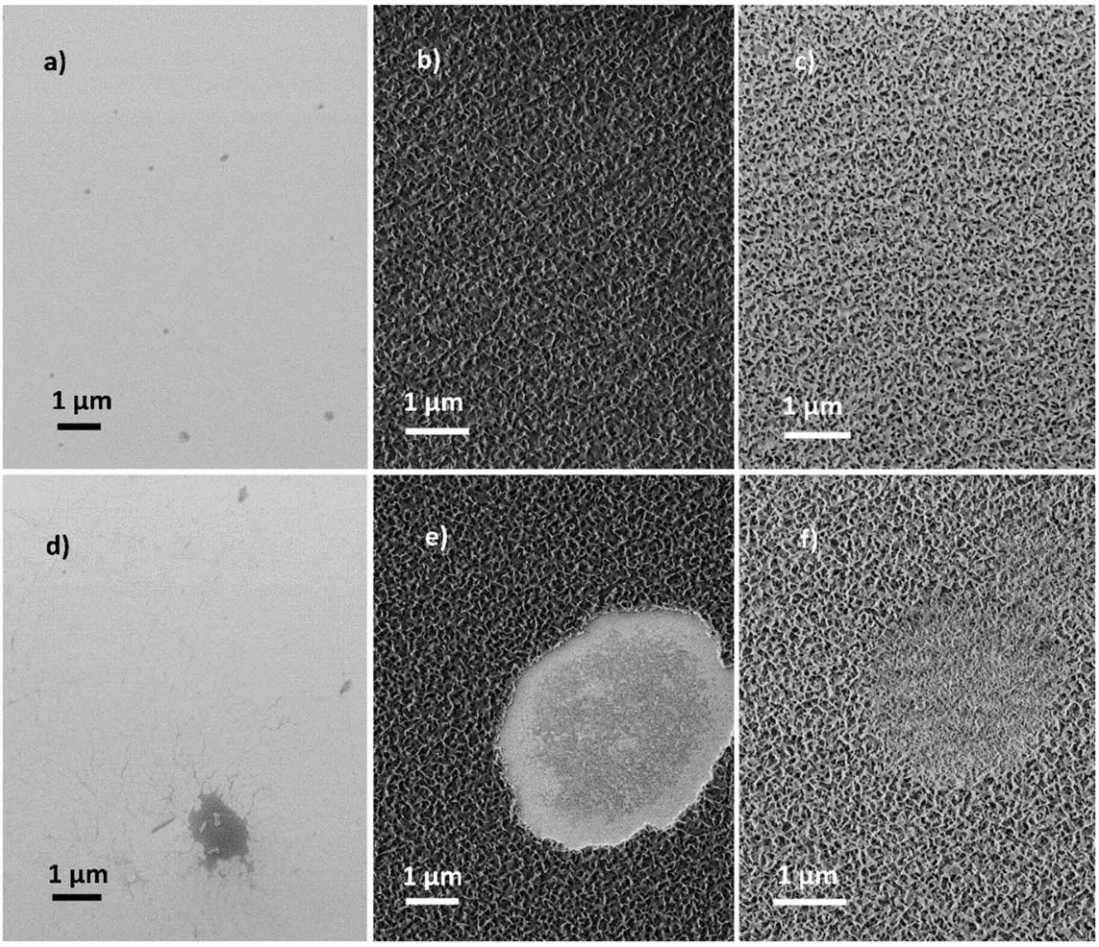

Figure 9. The scanning electron micrographs of alumina films on silicon. (a)–(c) show Plano, Nano and Fluoro surfaces pre-icing, respectively, and (d)–(f) show the same surfaces after the ice adhesion test.

the surface. It is likely that at the droplet impact stage the water drops have penetrated the coating [68], which combined with the freezing, seemingly leads to permanent coating damage. On Fluoro sample such peeled off areas are not found, and the substrate is still uniformly coated with the film. There are areas where the nanostructure has a visible dent very similar to the off-peeled areas on Nano, as shown in figure 9(f), but the water droplet has not penetrated the surface and caused delamination of the coating after the icing.

Results based on just one cycle of icing and de-icing by the centrifugal adhesion test might give a bit too optimistic view on the long-term capabilities of the samples in regards of anti-icing properties and durability. The samples that provided nearly unchanged performance (Plano and Fluoro on both substrates), were exposed to four additional icing and melting cycles and their hydrophobicity was examined with the contact angle measurements. Both the statistic and the dynamic contact angles are presented in figure 10(a) and the corresponding CA hysteresis is shown in figure 10(b).

The CA results after the cycling reveal that the hydrophobicity wears off for Fluoro samples whereas Plano surfaces have only small changes, most likely linked to the partial delamination seen in the SEM scans. This is in line with the similar cycling study of Farhadi *et al* where several different anti-icing nanocoatings were tested and found to lose their hydrophobic performance due to the cycling [28]. As stated by Kulinich *et al* [45] the surface state of the hydrophobic coating switches from the Cassie-Baxter to the Wenzel state due to the wear that the nanostructure undertakes during the cyclic icing and melting. The CA hysteresis in figure 10(b) shows that as the coatings are cyclically iced and de-iced the difference between ACA and RCA stabilizes around ~20° for both planar and hydrophobic nanostructured samples, which would indicate saturation of the wear on the nanostructure and roughening of the planar surface.

Despite not providing a permanent long-term protection against icing, the hydrophobic nanostructured alumina offers a durable and effective ARC to be used in conditions where atmospheric icing is not present. Such applications could be MJSC ARCs under a cover glass or specialized camera objectives, which already utilize subwavelength nanostructured films commercially [69]. The excellent transparency and extended durability

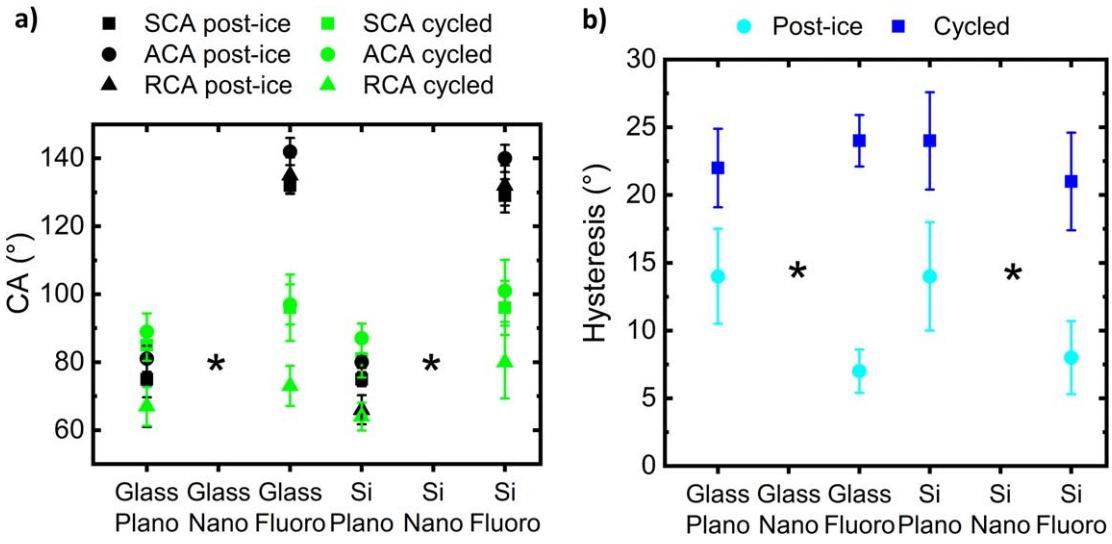

Figure 10. (a) The contact angles after the ice adhesion test and after four additional cycles of icing and melting the surfaces. (b) The contact angle hysteresis after ice adhesion test and after four additional cycles of icing and melting the surfaces. * Samples were not included in the additional icing-melting series.

when compared to the planar coating or only the nanostructured alumina, demonstrate the potential of hydrophobic nanostructured alumina for application in specialized broadband ARC solutions.

4. Conclusions

Nanostructured alumina antireflection coatings were hydrophobicity treated with CHF_3 plasma process and exposed to atmospheric icing for a durability assessment. The coating was compared to just nanostructured alumina and planar alumina coatings. The coatings were tested on both glass and silicon substrates. The effects of icing on the microstructure, the optical properties, and the wetting characteristics of the coatings were examined.

It was shown that just nanostructured alumina coating is superhydrophilic in nature and does not endure large environmental changes. The alumina nanostructure did not adhere on glass when the ice was removed by centrifugal adhesion test but peeled off leaving only residual nanostructures on the substrate. On silicon the adhesion was better, but the de-icing delaminated large pieces, with a diameter of tens of microns, of the coating. The planar coating was otherwise more durable and stable than the just nanostructured alumina, but it also had severe microcracks and off-peeled areas after the ice adhesion test. The fluoropolymerized hydrophobic nanostructured alumina provided high transmittance and possessed ice-phobic properties leaving the coating mostly unchanged after the centrifugal ice removal. The coating exceeded both the just nanostructured and planar coatings in durability and attained its hydrophobicity after the initial icing test. However, further cyclical icing/de-icing tests showed that even the hydrophobicity treated nanostructured alumina cannot withstand regular exposure to such conditions and the hydrophobic nature of the coating wears off.

The hydrophobic nanostructured alumina outperformed both the just nanostructured and planar alumina coatings and possessed increased durability and stability even under harsh conditions. This indicates a clear need to use a hydrophobicity treatment for the nanostructured alumina antireflection coatings even in regular indoor or controlled environments. Further development in the hydrophobicity treatment is required and other low surface energy polymers should be considered, not least because of the negative environmental effects of CHF_3. The challenge in this will be in attaining the excellent transmission properties, while simultaneously improving the hydrophobicity and durability of the coating.

Acknowledgments

This work made use of Tampere Microscopy Center facilities at Tampere University. The financial support provided by the European Research Council (ERC AdG AMETIST, #695116) is acknowledged. The work is also part of the Academy of Finland Flagship Program PREIN #320168. The icing tests were done as part of the Academy of Finland project 'Thermally Sprayed slippery liquid infused porous surface—towards durable anti-icing coatings' (TS-SLIPS) #317878.

Data availability statement

The data that support the findings of this study are available upon reasonable request from the authors.

ORCID iDs

Jarno Reuna https://orcid.org/0000-0003-0814-1740

References

[1] Kauppinen C, Isakov K and Sopanen M 2017 Grass-like alumina with low refractive index for scalable, broadband, omnidirectional antireflection coatings on glass using atomic layer deposition *ACS Appl. Mater. Interfaces* **9** 15038–43
[2] Reuna J, Aho A, Isoaho R, Raappana M, Aho T, Anttola E, Hietalahti A, Tukiainen A and Guina M 2021 Use of nanostructured alumina thin films in multilayer anti-reflective coatings *Nanotechnology* **32** 215602
[3] Reuna J, Hietalahti A, Aho A, Isoaho R, Aho T, Vuorinen M, Tukiainen A, Anttola E and Guina M 2022 Optical performance assessment of nanostructured alumina multilayer antireflective coatings used in III–V multijunction solar cells *ACS Appl. Energy Mater.* **5** 5804–10
[4] Yin C, Zhu M, Zeng T, Sun J, Zhang R, Zhao J, Wang L and Shao J 2021 Al2O3 anti-reflection coatings with graded-refractive index profile for laser applications *Opt. Mater. Express* **11** 875
[5] Isakov K, Kauppinen C, Franssila S and Lipsanen H 2020 Superhydrophobic antireflection coating on glass using grass-like alumina and fluoropolymer *ACS Appl. Mater. Interfaces* **12** 49957–62
[6] Sutha S, Suresh S, Raj B and Ravi K R 2017 Transparent alumina based superhydrophobic self—cleaning coatings for solar cell cover glass applications *Solar Energy Materials and Solar Cells* **165** 128–137
[7] Omrani M K, Malekmohammad M and Zabolian H 2022 Wide-angle broadband antireflection coatings based on boomerang-like alumina nanostructures in visible region *Sci. Rep.* **12** 1–8
[8] Zhou W, Tao M, Chen L and Yang H 2007 Microstructured surface design for omnidirectional antireflection coatings on solar cells *J. Appl. Phys.* **102** 103105
[9] Sun C-H, Ho B J, Jiang B and Jiang P 2008 Biomimetic subwavelength antireflective gratings on GaAs *Opt. Lett.* **33** 2224
[10] Tommila J, Polojärvi V, Aho A, Tukiainen A, Viheriälä J, Salmi J, Schramm A, Kontio J M, Turtiainen A and Niemi T 2010 Nanostructured broadband antireflection coatings on AlInP fabricated by nanoimprint lithography *Sol. Energy Mater. Sol. Cells* **94** 1845–8
[11] Tommila J, Aho A, Tukiainen A, Polojärvi V, Salmi J, Niemi T and Guina M 2013 Moth-eye antireflection coating fabricated by nanoimprint lithography on 1 eV dilute nitride solar cell *Prog. Photovoltaics Res. Appl.* **21** 1158–62
[12] Liang D, Kang Y, Huo Y, Chen Y, Cui Y and Harris J S 2013 High-efficiency nanostructured window GaAs solar cells *Nano Lett.* **13** 4850–6
[13] Leem J W, Yu J S, Heo J, Park W K, Park J H, Cho W J and Kim D E 2014 Nanostructured encapsulation coverglasses with wide-angle broadband antireflection and self-cleaning properties for III-V multi-junction solar cell applications *Sol. Energy Mater. Sol. Cells* **120** 555–60
[14] Leem J W, Su Y J, Jun D H, Heo J and Park W K 2014 Efficiency improvement of III-V GaAs solar cells using biomimetic TiO_2 subwavelength structures with wide-angle and broadband antireflection properties *Sol. Energy Mater. Sol. Cells* **127** 43–9
[15] Perl E E, Lin C T, McMahon W E, Friedman D J and Bowers J E 2014 Ultrabroadband and wide-angle hybrid antireflection coatings with nanostructures *IEEE J. Photovoltaics* **4** 962–7
[16] Perl E E, McMahon W E, Bowers J E and Friedman D J 2014 Design of antireflective nanostructures and optical coatings for next-generation multijunction photovoltaic devices *Opt. Express* **22** A1243
[17] Abdulagatov A I, Yan Y, Cooper J R, Zhang Y, Gibbs Z M, Cavanagh A S, Yang R G, Lee Y C and George S M 2011 Al_2O_3 and TiO_2 atomic layer deposition on copper for water corrosion resistance *ACS Appl. Mater. Interfaces* **3** 4593–601
[18] Kim L H, Kim K, Park S, Jeong Y J, Kim H, Chung D S, Kim S H and Park C E 2014 Al_2O_3/TiO_2 nanolaminate thin film encapsulation for organic thin film transistors via plasma-enhanced atomic layer deposition *ACS Appl. Mater. Interfaces* **6** 6731–8
[19] Correa G C, Bao B and Strandwitz N C 2015 Chemical stability of titania and alumina thin films formed by atomic layer deposition *ACS Appl. Mater. Interfaces* **7** 14816–21
[20] Dokmai V, Methaapanon R and Pavarajarn V 2020 Corrosion of amorphous alumina in deionized water under mild condition *Appl. Surf. Sci.* **499** 143906
[21] Gottmann J and Kreutz E W 1999 Pulsed laser deposition of alumina and zirconia thin films on polymers and glass as optical and protective coatings *Surf. Coatings Technol.* **116–119** 1189–94
[22] Este G and Westwood W D 1984 Reactive deposition of low loss Al_2O_3 optical waveguides by modified dc planar magnetron sputtering *J. Vac. Sci. Technol. A Vacuum, Surfaces, Film.* **2** 1238–47
[23] Kischkat J *et al* 2012 Mid-infrared optical properties of thin films of aluminum oxide, titanium dioxide, silicon dioxide, aluminum nitride, and silicon nitride *Appl. Opt.* **51** 6789
[24] Tadanaga K, Katata N and Minami T 1997 Super-water-repellent Al_2O_3 coating films with high transparency *J. Am. Ceram. Soc.* **80** 1040–2
[25] Yamaguchi N, Tadanaga K, Matsuda A, Minami T and Tatsumisago M 2005 Anti-reflective coatings of flowerlike alumina on various glass substrates by the sol? Gel process with the hot water treatment *J. Sol-Gel Sci. Technol.* **33** 117–20
[26] Tadanaga K, Katata N and Minami T 2005 Formation process of super-water-repellent Al_2O_3 coating films with high transparency by the sol-gel method *J. Am. Ceram. Soc.* **80** 3213–6
[27] Liu Z, Deng J and Li D 2000 A new tyrosinase biosensor based on tailoring the porosity of Al_2O_3 sol-gel to co-immobilize tyrosinase and the mediator *Anal. Chim. Acta* **407** 87–96
[28] Farhadi S, Farzaneh M and Kulinich S A 2011 Anti-icing performance of superhydrophobic surfaces *Appl. Surf. Sci.* **257** 6264–9
[29] Zhu T, Cheng Y, Huang J, Xiong J, Ge M, Mao J, Liu Z, Dong X, Chen Z and Lai Y 2020 A transparent superhydrophobic coating with mechanochemical robustness for anti-icing, photocatalysis and self-cleaning *Chem. Eng. J.* **399** 125746
[30] Allahdini A, Jafari R and Momen G 2022 Transparent non-fluorinated superhydrophobic coating with enhanced anti-icing performance *Prog. Org. Coatings* **165** 106758

[31] Kulinich S A and Farzaneh M 2011 On ice-releasing properties of rough hydrophobic coatings *Cold Reg. Sci. Technol.* **65** 60–4
[32] Yang S, Xia Q, Zhu L, Xue J, Wang Q and Chen Q M 2011 Research on the icephobic properties of fluoropolymer-based materials *Appl. Surf. Sci.* **257** 4956–62
[33] Momen G, Jafari R and Farzaneh M 2015 Ice repellency behaviour of superhydrophobic surfaces: effects of atmospheric icing conditions and surface roughness *Appl. Surf. Sci.* **349** 211–8
[34] Binh N T, Hanh V T H, Ngoc N T and Duc N B 2021 Anti-icing efficiency on bio-inspired slippery elastomer surface *Mater. Chem. Phys.* **265** 124502
[35] Drábik M, Polonskyi O, Kylián O, Čechvala J, Artemenko A, Gordeev I, Choukourov A, Slavínská D, Matolínová I and Biederman H 2010 Super-hydrophobic coatings prepared by RF magnetron sputtering of PTFE *Plasma Process. Polym.* **7** 544–51
[36] Han W, Li Y, Tang H and Liu H 2012 Treatment of the potent greenhouse gas, CHF3—an overview *J. Fluor. Chem.* **140** 7–16
[37] Rodgers K M, Swartz C H, Occhialini J, Bassignani P, McCurdy M and Schaider L A 2021 How well do product labels indicate the presence of PFAS in consumer items used by children and adolescents? *Environ. Sci. Technol.* **56** 6294–304
[38] Liu Z, Chen Z, Gao J, Yu Y, Men Y, Gu C and Liu J 2022 Accelerated degradation of perfluorosulfonates and perfluorocarboxylates by UV/Sulfite + iodide: reaction mechanisms and system efficiencies *Environ. Sci. Technol.* **56** 3699–709
[39] Fillion R M, Riahi A R and Edrisy A 2014 A review of icing prevention in photovoltaic devices by surface engineering *Renew. Sustain. Energy Rev.* **32** 797–809
[40] Jung S, Dorrestijn M, Raps D, Das A, Megaridis C M and Poulikakos D 2011 Are superhydrophobic surfaces best for icephobicity? *Langmuir* **27** 3059–66
[41] Chen J, Liu J, He M, Li K, Cui D, Zhang Q, Zeng X, Zhang Y, Wang J and Song Y 2012 Superhydrophobic surfaces cannot reduce ice adhesion *Appl. Phys. Lett.* **101** 18–21
[42] Nosonovsky M and Hejazi V 2012 Why superhydrophobic surfaces are not always icephobic *ACS Nano* **6** 8488–91
[43] Varanasi K K, Deng T, Smith J D, Hsu M and Bhate N 2010 Frost formation and ice adhesion on superhydrophobic surfaces *Appl. Phys. Lett.* **97** 95–8
[44] Oberli L, Caruso D, Hall C, Fabretto M, Murphy P J and Evans D 2014 Condensation and freezing of droplets on superhydrophobic surfaces *Adv. Colloid Interface Sci.* **210** 47–57
[45] Kulinich S A, Farhadi S, Nose K and Du X W 2011 Superhydrophobic surfaces: are they really ice-repellent? *Langmuir* **27** 25–9
[46] Koivuluoto H, Stenroos C, Ruohomaa R, Bolelli G, Lusvarghi L and Vuoristo P 2015 Research on icing behavior and ice adhesion testing of icephobic surfaces *Proc. 16th Int. Work. Atmos. Icing Struct. IWAIS XVI (Jun 28–Jul 31–14*
[47] Koivuluoto H, Hartikainen E and Niemelä-Anttonen H 2020 Thermally sprayed coatings: novel surface engineering strategy towards icephobic solutions *Materials (Basel).* **13** 1434
[48] Niemelä-Anttonen H *et al* 2018 Icephobicity of slippery liquid infused porous surfaces under multiple freeze–thaw and ice accretion–detachment cycles *Adv. Mater. Interfaces* **5** 1–8
[49] Donadei V, Koivuluoto H, Sarlin E, Niemelä-Anttonen H, Varis T and Vuoristo P 2022 The effect of mechanical and thermal stresses on the performance of lubricated icephobic coatings during cyclic icing/deicing tests *Prog. Org. Coatings* **163** 106614
[50] Horcas I, Fernández R, Gómez-Rodríguez J M, Colchero J, Gómez-Herrero J and Baro A M 2007 WSXM: a software for scanning probe microscopy and a tool for nanotechnology *Rev. Sci. Instrum.* **78** 1–8
[51] Young T 1805 III. An essay on the cohesion of fluids *Philos. Trans. R. Soc. London* **95** 65–87
[52] Law K-Y 2014 Definitions for hydrophilicity, hydrophobicity, and superhydrophobicity: getting the basics right *J. Phys. Chem. Lett.* **5** 686–8
[53] Drelich J and Chibowski E 2010 Superhydrophilic and superwetting surfaces: definition and mechanisms of control *Langmuir* **26** 18621–3
[54] Wenzel R N 1936 Resistance of solid surfaces to wetting by water *Ind. Eng. Chem.* **28** 988–94
[55] Wenzel R N 1949 Surface roughness and contact angle *J. Phys. Colloid Chem.* **53** 1466–7
[56] Cassie A B D and Baxter S 1944 Wettability of porous surfaces *Trans. Faraday Soc.* **40** 546
[57] Extrand C W 2002 Model for contact angles and hysteresis on rough and ultraphobic surfaces *Langmuir* **18** 7991–9
[58] Quéré D 2008 Wetting and roughness *Annu. Rev. Mater. Res.* **38** 71–99
[59] Hansson P M, Hormozan Y, Brandner B D, Linnros J, Claesson P M, Swerin A, Schoelkopf J, Gane P A C and Thormann E 2013 Hydrophobic pore array surfaces: wetting and interaction forces in water/ethanol mixtures *J. Colloid Interface Sci.* **396** 278–86
[60] Wu X, Tang Y, Silberschmidt V V, Wilson P and Chen Z 2018 Mechanically robust transparent anti-icing coatings: roles of dispersion status of titanate nanotubes *Adv. Mater. Interfaces* **5** 1–10
[61] Samuel B, Zhao H and Law K Y 2011 Study of wetting and adhesion interactions between water and various polymer and superhydrophobic surfaces *J. Phys. Chem.* C **115** 14852–61
[62] Marmur A 1994 Thermodynamic aspects of contact angle hysteresis *Adv. Colloid Interface Sci.* **50** 121–41
[63] Gao L and McCarthy T J 2006 Contact angle hysteresis explained *Langmuir* **22** 6234–7
[64] Aiken D J 2000 Antireflection coating design for series interconnected multi-junction solar cells *Prog. Photovoltaics Res. Appl.* **8** 563–70
[65] Guter W, Schöne J, Philipps S P, Steiner M, Siefer G, Wekkeli A, Welser E, Oliva E, Bett A W and Dimroth F 2009 Current-matched triple-junction solar cell reaching 41.1% conversion efficiency under concentrated Sunlight *Appl. Phys. Lett.* **94** 8–11
[66] Rosamilia J M, Boone T, Sapjeta J, Raghavachari K, Higashi G S and Liu Q 1997 Hot water etching of silicon surfaces: new insights of mechanistic understanding and implications to device fabrication *Mater. Res. Soc. Symp. - Proc.* **477** 181–90
[67] Wu X, Silberschmidt V V, Hu Z T and Chen Z 2019 When superhydrophobic coatings are icephobic: role of surface topology *Surf. Coatings Technol.* **358** 207–14
[68] Sun T, Álvarez-Novoa F, Andrade K, Gutiérrez P, Gordillo L and Cheng X 2022 Stress distribution and surface shock wave of drop impact *Nat. Commun.* **13** 1703
[69] Okuno T 2010 Development of subwavelength structure coating (SWC) and its application to imaging lenses *International Optical Design Conference and Optical Fabrication and Testing* (Washington, DC: OSA) p IMA2